

# StructuredField: Unifying Structured Geometry and Radiance Field

KAIWEN SONG, University of Science and Technology of China, China

JINKAI CUI, University of Science and Technology of China, China

ZHERUI QIU, University of Science and Technology of China, China

JUYONG ZHANG, University of Science and Technology of China, China

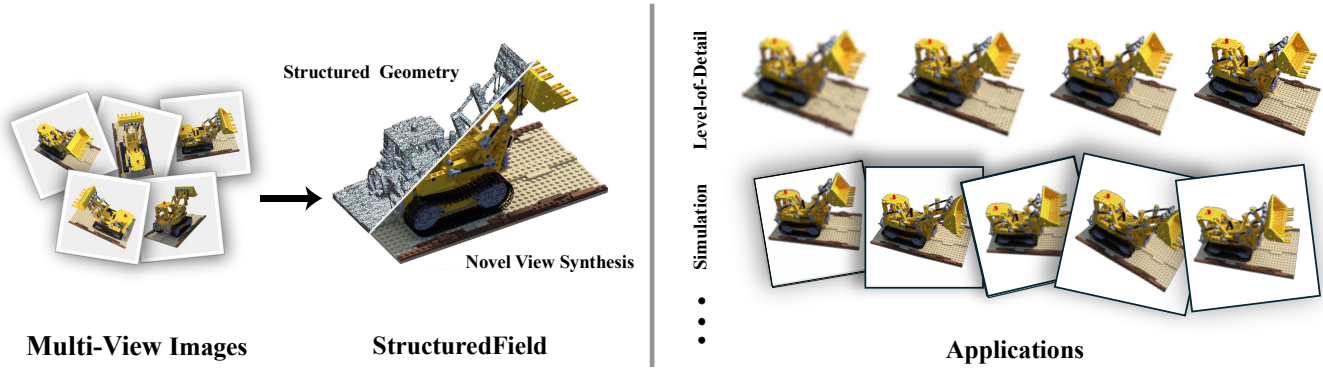


Fig. 1. **StructuredField** represents and reconstructs scene using a structured tetrahedral mesh. This novel structured 3D representation enables a variety of applications, including physical simulations, deformations, and more.

Recent point-based differentiable rendering techniques have achieved significant success in high-fidelity reconstruction and fast rendering. However, due to the unstructured nature of point-based representations, they are difficult to apply to modern graphics pipelines designed for structured meshes, as well as to a variety of simulation and editing algorithms that work well with structured mesh representations. To this end, we propose StructuredField, a novel representation that achieves both a structured geometric representation of the reconstructed object and high-fidelity rendering reconstruction. We employ structured tetrahedral meshes to represent the reconstructed object. We reparameterize the geometric attributes of these tetrahedra into the parameters of 3D Gaussian primitives, thereby enabling differentiable, high-fidelity rendering directly from the mesh. Furthermore, a hierarchical implicit subdivision strategy is utilized to ensure a conformal mesh structure while empowering the representation to capture multi-scale details. To maintain geometric integrity during optimization, we propose a novel inversion-free homeomorphism that constrains the tetrahedral mesh, guaranteeing it remains both inversion-free and self-intersection-free during the optimization process and in the final result. Based on our proposed StructuredField, we achieve high-quality structured meshes that are completely inversion-free and conformal, while also attaining reconstruction results comparable to those of 3DGS. We also demonstrate the applicability of our representation to various applications such as physical simulation, deformation, and level-of-detail. Code available at <https://github.com/kevin2000A/StructuredField>.

Authors' Contact Information: Kaiwen Song, [sa21001046@mail.ustc.edu.cn](mailto:sa21001046@mail.ustc.edu.cn), University of Science and Technology of China, Hefei, Anhui, China; Jinkai Cui, [cuijk@mail.ustc.edu.cn](mailto:cuijk@mail.ustc.edu.cn), University of Science and Technology of China, Hefei, Anhui, China; Zherui Qiu, [zrqiu@mail.ustc.edu.cn](mailto:zrqiu@mail.ustc.edu.cn), University of Science and Technology of China, Hefei, Anhui, China; Juyong Zhang, [juyong@ustc.edu.cn](mailto:juyong@ustc.edu.cn), University of Science and Technology of China, Hefei, Anhui, China.

© 2025 Copyright held by the owner/author(s). Publication rights licensed to ACM. This is the author's version of the work. It is posted here for your personal use. Not for redistribution. The definitive Version of Record was published in *ACM Transactions on Graphics*, <https://doi.org/10.1145/nnnnnnn.nnnnnnn>.

CCS Concepts: • **Computing methodologies** → **Rendering; Rasterization; Volumetric models.**

Additional Key Words and Phrases: tetrahedral mesh, radiance fields, physics simulation, 3D reconstruction, differentiable rendering

## ACM Reference Format:

Kaiwen Song, Jinkai Cui, Zherui Qiu, and Juyong Zhang. 2025. StructuredField: Unifying Structured Geometry and Radiance Field. *ACM Trans. Graph.* 1, 1 (August 2025), 15 pages. <https://doi.org/10.1145/nnnnnnn.nnnnnnn>

## 1 Introduction

Photorealistic and real-time rendering of 3D scenes is a central pursuit in computer graphics, both in academic research and practical applications. Traditional 3D representations, such as meshes [Botsch et al. 2005; Hoppe 2002; Liu et al. 2019] and point clouds [Rusinkiewicz and Levoy 2000; Yifan et al. 2019], facilitate real-time rendering through rasterization techniques that align with modern GPU rendering architectures. Nevertheless, these methods frequently produce low-quality rendering, exhibiting missing geometric details and blurry artifacts. In contrast, emerging differentiable volumetric rendering methods [Barron et al. 2021; Chen et al. 2022; Müller et al. 2022], including neural radiance fields [Mildenhall et al. 2020a], demonstrate the capability to reconstruct 3D scenes in an end-to-end manner using multi-view images, thus achieving high fidelity and maintaining intricate details. However, the reliance on ray tracing-based rendering pipelines and the necessity for extensive sampling points pose challenges to rapid rendering in NeRF variants.

Recently, advancements in point-based differentiable rendering techniques [Held et al. 2024; Huang et al. 2024b,a; Kerbl et al. 2023] have demonstrated notable success in enhancing both rendering speed and high-fidelity reconstruction by leveraging smooth primitives within rasterization-based pipelines. While these point-based

rendering techniques offer numerous advantages, they inherently represent scenes as unstructured point clouds. In contrast, contemporary graphics pipelines are predominantly designed for structured representations, such as polygonal meshes. These structured forms are widely adopted in a variety of applications, including animation [James and Twigg 2005; Sorkine and Alexa 2007], physical simulation [Ando et al. 2013; Baraff and Witkin 2023; Liu et al. 2013], and editing [Yu et al. 2004; Zorin et al. 1997], where an explicit and coherent geometric structure is essential. Consequently, the absence of such inherent object structure in point-based methods significantly constrains their broader applicability.

Our primary aim in this study is to bridge the gap between recent high-fidelity differentiable point-based representations and traditional graphics pipelines tailored for structured meshes. To this end, we introduce StructuredField, a novel method that unifies high-fidelity differentiable rendering and high-quality structured geometry. Our fundamental representation within StructuredField is the tetrahedral mesh, as it is suited for volumetric data and has been widely utilized in volume rendering [Ma and Crockett 1997; Weiler et al. 2003; Yagel et al. 1996]. To enable high-fidelity visual reconstruction, StructuredField reparameterizes the attributes of 3D Gaussian primitives with the geometric parameters of the underlying tetrahedral mesh. This strategy facilitates the direct, end-to-end differentiable optimization of the tetrahedral mesh using image-based losses, thereby achieving detailed reconstruction and high-quality rendering.

However, directly optimizing the vertex positions of tetrahedral meshes can readily lead to anomalous geometric structures, such as self-intersections or element inversions. To prevent these issues and ensure the integrity of the geometric structure throughout the optimization process, we analyze two main causes of mesh anomalies: self-intersections and element inversions, and propose a novel orientation-preserving homeomorphism [Behrmann et al. 2019; Dinh et al. 2017], which constrains the feasible deformation space of the mesh vertices, strictly maintaining a valid, intersection-free, and inversion-free tetrahedral mesh.

Furthermore, the capacity of a 3D representation to capture multi-scale details, like multi-resolution hash encodings in InstantNGP [Müller et al. 2022] and adaptive density control in 3D Gaussian Splatting [Kerbl et al. 2023], is fundamental for achieving high-fidelity reconstruction. However, when extending to tetrahedral representations, achieving operations similar to adaptive density control often requires explicit, multi-level subdivision of the tetrahedra. Such explicit subdivision inherently introduces non-conformal interfaces between tetrahedral elements, which are problematic for downstream applications like physical simulation. Instead, we utilize an implicit subdivision strategy that adaptively refines regions for rendering by introducing implicit child tetrahedra without modifying the fixed topology of the initial conformal mesh. Consequently, by applying these two strategies, our representation inherently ensures high-quality geometry for simulation while providing sufficient expressive power for high-fidelity reconstruction.

Through comprehensive experimentation, we demonstrate that our approach achieves rendering quality comparable to or even exceeding that of recent point-based rendering techniques. Furthermore, our representation can be seamlessly integrated into various

applications like physics simulation and deformation without necessitating algorithmic redesigns or extensive modifications. Our primary contributions can be summarized as:

- We introduce StructuredField, a novel 3D representation that seamlessly combines structured tetrahedral geometry with high-fidelity differentiable rendering capabilities through the reparameterization of 3D Gaussian functions.
- We design a novel orientation-preserving homeomorphism constraint to ensure that the tetrahedral mesh remains inversion-free and self-intersection-free during optimization.
- We propose an implicit subdivision strategy for tetrahedral meshes that maintains a high-quality base mesh structure suitable for physical simulations while ensuring adaptive multi-scale details for high-fidelity reconstructions.

## 2 Related work

### 2.1 3D Reconstruction

Reconstructing 3D scenes from multi-view images is a longstanding problem in both computer graphics and computer vision. Traditional 3D reconstruction techniques include Structure-from-Motion (SfM) pipelines [Agarwal et al. 2009; Frahm et al. 2010] to estimate camera poses and obtain sparse point clouds, followed by surface reconstruction through dense multi-view stereo [Furukawa et al. 2010; Furukawa and Ponce 2010; Jin et al. 2005]. These methods rely on hand-crafted features to acquire fine textures and geometry, and struggle to reconstruct view-dependent colors. Significant advancements have been achieved in NVS, particularly since the introduction of Neural Radiance Fields (NeRF) [Mildenhall et al. 2020a]. The original NeRF represents the scene as an MLP, which maps positional encodings of spatial locations and directions to attributes including color and density, and utilizes a volume rendering process to achieve realistic rendering. Various works have enhanced the performance of NeRF [Barron et al. 2021, 2023; Müller et al. 2022] or extended them to large scenes [Barron et al. 2022; Tancik et al. 2022]. More recently, 3DGS [Kerbl et al. 2023] optimizes anisotropic 3D Gaussian primitives, demonstrating real-time photorealistic reconstruction results. This method has been rapidly extended to multiple domains [Keetha et al. 2024; Lin et al. 2024; Tang et al. 2024; Xiang et al. 2024]. Despite these successes, point-based representations are unstructured, limiting their further applications. In this paper, we demonstrate detailed reconstruction while maintaining a structured tetrahedral mesh, and showcase its subsequent applications.

### 2.2 Mesh-based Representation

Explicit representations have served as a cornerstone within 3D modeling and computer graphics for decades [Woo et al. 1999]. Conventional geometric representations like point clouds, voxels and polygonal meshes have been extensively revisited in the context of 3D deep learning. Polygonal meshes are particularly attractive due to their structured geometry and efficient rendering properties. Recently, differentiable rendering methods [Liu et al. 2019; Pihorskyi et al. 2025] leveraging mesh representations have enabled the production of high-quality renderings. However, the optimization processes inherent to mesh representations are often hampered by rigid topological constraints, resulting in limited flexibility and

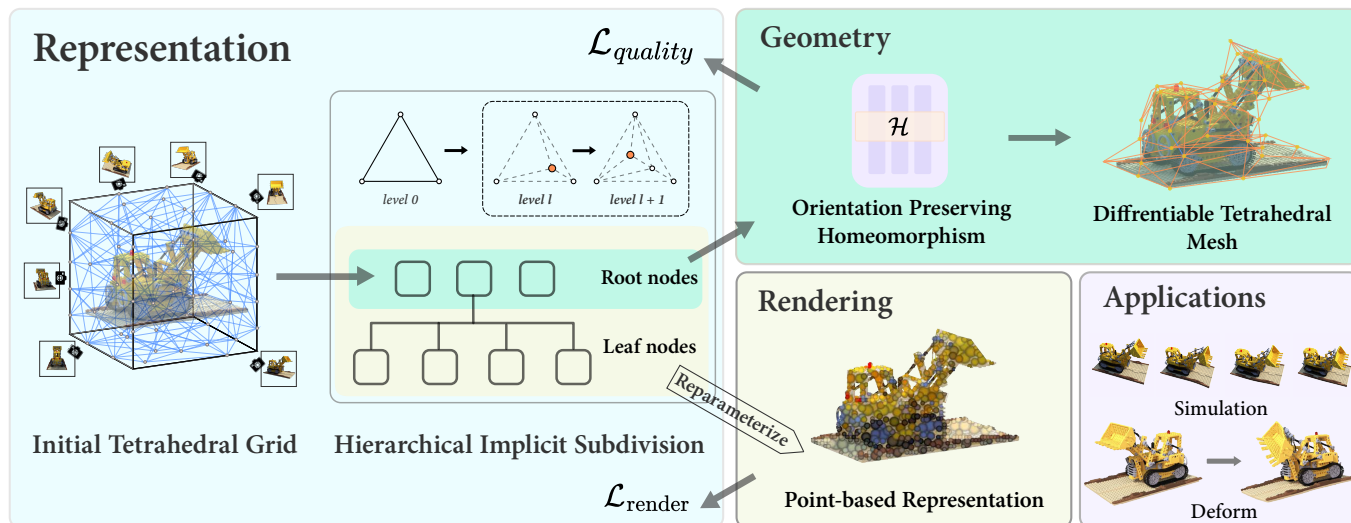


Fig. 2. **Overview of StructuredField.** Given multi-view images as input, we reconstruct the 3D scene using a structured tetrahedral mesh. Our implicit multi-level subdivision module iteratively refines the initial input tetrahedra, creating a hierarchical structure. The root nodes of this hierarchy (the base tetrahedra) form a high-quality geometric foundation; their vertex positions are optimized using an orientation-preserving homeomorphism to maintain an inversion-free and robustly structured geometry, which supports subsequent applications. The leaf node tetrahedra, capturing the finest adaptive details, are then reparameterized into 3D Gaussian Splatting (3DGS) primitives for high-fidelity differentiable rendering. Based on our structured mesh representation, the reconstructed model can be further applied to physical simulations, deformation, and other graphics applications.

reduced capacity to accurately depict realistic appearances. Our method integrates inversion-free mapping to effectively regulate and maintain structural integrity during the mesh optimization process while ensuring high quality reconstruction, addressing these limitations.

On the other hand, NeRF [Mildenhall et al. 2020b] has attracted considerable attention due to their ability to deliver high-fidelity renderings. Substantial research has focused on integrating implicit methods with mesh structures to extend and refine NeRF [Wang et al. 2021]. For instance, some approaches [Turki et al. 2024; Wan et al. 2023; Wang et al. 2023b] utilize meshes to constrain the sampling regions within an adaptively learned narrow band of two explicit meshes. On the other hand, Tetra-NeRF [Kulhanek and Sattler 2023; Rosu and Behnke 2023] employs tetrahedral meshes as feature grids to accelerate the training process. Additionally, leveraging the fast rendering capabilities of meshes, Baked SDF and its variants [Reiser et al. 2024; Yariv et al. 2023] have baked radiance fields into meshes to facilitate real-time rendering. Mesh representations have also been pivotal in the deformation of radiance fields. NeRFShop and Cage-NeRF [Jambon et al. 2023; Peng et al. 2022] use meshes as cages to drive the deformation of radiance fields.

Recently, point-based representations [Huang et al. 2024b,a; Kerbl et al. 2023] have emerged, utilizing smooth primitives to represent radiance fields and employing rasterization techniques to accelerate rendering. In subsequent works, Mani-gs and GaMes [Gao et al. 2024] employ high-quality triangle meshes or triangle soups as proxies, binding primitives to the triangle mesh to drive the deformation of 3D Gaussians. Additionally, VR-GS [Jiang et al. 2024] and D3GA [Zielonka et al. 2025] adopt tetrahedral meshes as proxies

to facilitate the deformation of objects. However, these methods directly bind the mesh to Gaussians without optimizing the positions of the mesh vertices. As a result, any imperfections in the initial mesh can significantly degrade the final reconstruction quality. In contrast, our method reparameterizes Gaussians with tetrahedral mesh vertices and optimizes these vertices, thereby allowing for high-quality reconstruction.

### 2.3 Inversion-free Mesh Optimization

Maintaining mesh quality during the optimization process remains a challenging problem. Element inversion is a major factor causing mesh quality issues [Fu et al. 2021]. Traditional methods [Rabinovich et al. 2017; Schüller et al. 2013] impose constraints on the Jacobian of the mapping during optimization to ensure the Jacobian remains positive, thereby enforcing that the mapping is orientation-preserving. In addition to being inversion-free, intersection-free boundaries are also necessary during the optimization. This is typically achieved by constraining the mapping to be bijective. Traditional methods [Jiang et al. 2017; Misztal and Bærentzen 2012] introduce scaffold meshes to convert the globally overlap-free constraint into a locally flip-free condition. Recently, invertible networks [Behrmann et al. 2019; Dinh et al. 2017] offer another solution, leading to their widespread adoption in recent 3D deformation tasks. For instance, NDR [Cai et al. 2022] and Cadex [Lei and Daniilidis 2022] employ invertible networks to model the motion of objects, thereby achieving dynamic object reconstruction. NFGP [Yang et al. 2021] utilizes invertible networks to perform geometric processing on implicit surfaces. Compared to these methods, we propose a novel invertible network that implicitly and strictly constrains the mapping to be inversion-free

and intersection-free, and apply it during the optimization process to guarantee the mesh quality.

### 3 Method

Given multi-view posed images of a scene, our primary objective is to reconstruct it with high fidelity and high-quality geometry. This enables seamless integration of the reconstructed 3D scene into existing computer graphics pipelines for applications such as rendering, animation, physical simulation, and deformation. To this end, we first introduce a novel tetrahedral mesh-based 3D representation that is structurally organized and facilitates differentiable optimization (Sec. 3.1). The mesh is optimized using an orientation-preserving homeomorphism to ensure high-quality structured geometry (Sec. 3.3). We further introduce a hierarchical implicit subdivision scheme to achieve conformal geometry while enabling multi-scale rendering detail (Sec. 3.2). An overview of our representation and reconstruction pipeline is shown in Fig. 2.

#### 3.1 Representation of StructuredField

Given a tetrahedral mesh  $\mathcal{M} = (\mathcal{V}, \mathcal{T})$ , where  $\mathcal{V} = \{v_i\}_{i=1}^N$  represents the set of vertices,  $\mathcal{T} = \{T_k\}_{k=1}^K$  is the set of tetrahedron. Each tetrahedron  $T_k \in \mathcal{T}$  is defined by four vertices  $\{v_{k_1}, v_{k_2}, v_{k_3}, v_{k_4}\}$ . Tetrahedral meshes are generally challenging to render in a differentiable manner due to their discrete, non-smooth nature.

To address this limitation, we build upon recent point-based differentiable rendering techniques, such as 3D Gaussian Splatting (3DGS) [Kerbl et al. 2023], 2D Gaussian Splatting (2DGS) [Huang et al. 2024b], and convex splatting [Held et al. 2024]. In our method, we establish a one-to-one correspondence between each tetrahedron and a primitive, using a differentiable reparameterization function  $F_r(\cdot)$  to map the parameters  $T_k$  of the tetrahedron to the parameters  $\Theta_k$  of the primitive:

$$\Theta_k = F_r(T_k). \quad (1)$$

The gradients are propagated back to the parameters of tetrahedra through the differentiable reparameterization function, enabling the optimization of vertex positions and associated attributes in a fully differentiable framework. In the following, we demonstrate how the parameters of 3DGS can be reparameterized using the parameters of a tetrahedral mesh.

*Reparameterize 3D Gaussians.* 3DGS [Kerbl et al. 2023] represents a scene with a set of 3D Gaussians  $\mathcal{G} = \{g_k\}_{k=1}^K$ , where each Gaussian  $g_k$  encodes the following attributes: mean  $\mu_k \in \mathbb{R}^3$ , scales  $s_k \in \mathbb{R}^3$ , rotation  $r_k \in \mathbb{R}^4$ , color  $c_k \in \mathbb{R}^3$ , and opacity  $o_k \in \mathbb{R}$ . In our representation, each tetrahedron  $T_k$  contains four vertices with positions  $\{v_{k_i}\}_{i=1}^4$ , spherical harmonic coefficients  $\{\text{SH}_{k_i}\}_{i=1}^4$ , and weights  $\{w_{k_i}\}_{i=1}^4$ . We first compute the mean  $\mu_k$  and an initial, PCA-derived covariance matrix  $\Sigma'_k$  from the weighted vertex positions of  $T_k$ , following a PCA-style approach [Abdi and Williams 2010]:

$$\mu_k = \frac{\sum_{i=1}^4 w_{k_i} v_{k_i}}{\sum_{i=1}^4 w_{k_i}}, \quad \Sigma'_k = \sum_{i=1}^4 w_{k_i} (v_{k_i} - \mu_k)(v_{k_i} - \mu_k)^\top. \quad (2)$$

This  $\Sigma'_k$  captures the initial anisotropic shape implied by the vertex distribution of  $T_k$ . The optimizable quaternion  $q_k$  is converted to its corresponding rotation matrix  $\Delta R_k$ . The final anisotropic covariance

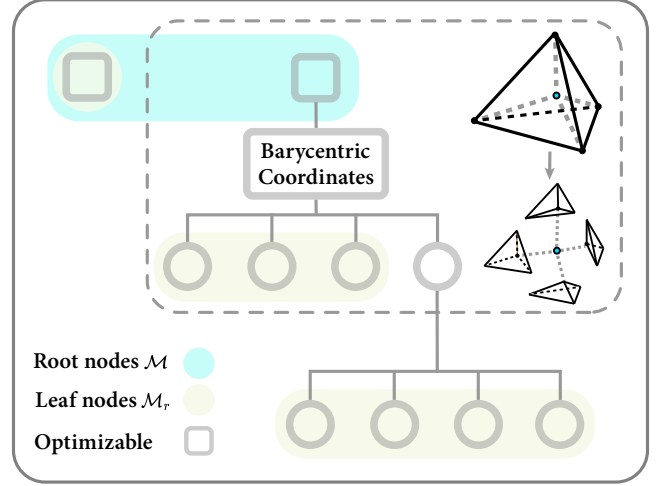


Fig. 3. **Data Structure of Hierarchical Implicit Subdivision.** Base tetrahedra can be iteratively subdivided in a 1-to-4 manner, forming a quadtree-like hierarchy. The root node tetrahedra constitute a high-quality and conformal geometry, designated for downstream applications such as physical simulation. Leaf node tetrahedra are utilized for high-quality rendering. The positions of the implicitly defined subdivision control points are optimized via their barycentric coordinates within their respective parent tetrahedra, while the positions of the root node vertices are optimized using our Orientation-preserving Homeomorphism.

matrix  $\Sigma_k$  for the 3D Gaussian is then obtained by applying this learned rotation:

$$\Sigma_k = \Delta R_k \Sigma'_k \Delta R_k^T. \quad (3)$$

This explicit, optimizable rotation allows the 3D Gaussian primitive to more flexibly orient itself to fit the local scene content associated with  $T_k$ .

The opacity attribute  $o_k$  is defined on the tetrahedron instead of on the vertices, so the opacity of its corresponding Gaussian is equivalent to the opacity of the tetrahedron. The color of the Gaussian is obtained by a weighted average of the colors computed from the spherical harmonic function of each vertex:

$$c = \frac{\sum_{i=1}^4 w_i c_i}{\sum_{i=1}^4 w_i}, \quad c_i = \text{SH}_i(\mathbf{d}), \quad (4)$$

where  $\mathbf{d}$  is the direction from the camera center to the vertex.

After reparameterizing 3D Gaussians with tetrahedral mesh, the scene can be rendered in a differentiable manner. However, freely optimizing the tetrahedral vertices leads to low-quality tetrahedral mesh, as shown in Fig. 6. In Section 3.3, we introduce the orientation-preserving homeomorphism to address this issue.

#### 3.2 Hierarchical Implicit subdivision

High-fidelity rendering often requires capturing details at multiple scales, a capability demonstrated by many successful 3D reconstruction methods. For example, Instant-NGP [Müller et al. 2022] uses multi-resolution hash encodings, combining features from various grid resolutions to efficiently represent intricate, multi-scale details.

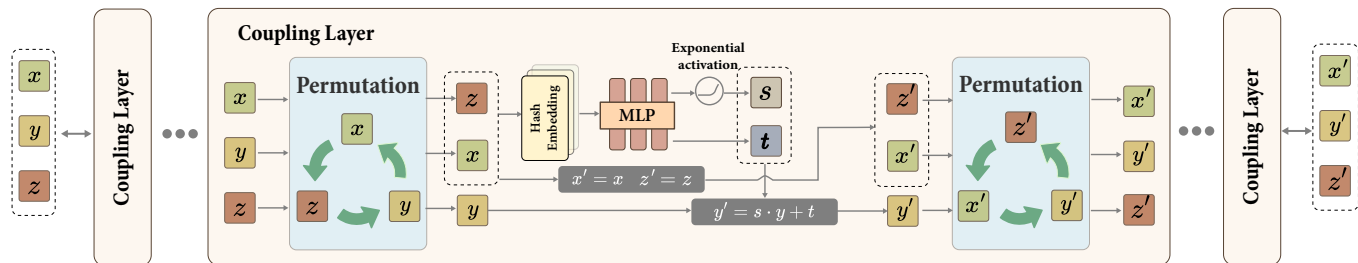


Fig. 4. **Invertible neural network architecture.** By applying a permutation strategy, the input vector is divided into two contiguous parts, ensuring that the resulting Jacobian matrix is upper triangular with positive diagonal elements. This strategy guarantees that the determinant of the Jacobian is positive, thus ensuring that the mapping is inversion-free.

Similarly, 3D Gaussian Splatting [Kerbl et al. 2023] employs adaptive density control, refining Gaussian primitives in under reconstructed regions to better capture fine-scale information. Therefore, to equip our tetrahedral representation with a comparable capability to capture details across diverse scales, a mechanism for refining the tetrahedral elements themselves is essential.

While explicitly subdividing tetrahedra in the base mesh  $\mathcal{M}$  can introduce finer geometric details, this direct modification of the mesh topology often creates non-conformal interfaces or degenerate elements. Such non-conformality and the presence of degenerate or ill-conditioned elements are highly problematic for downstream applications like physical simulation, which demand well-structured, conformal meshes, and also invariably increase the complexity of the simulation mesh. To circumvent these drawbacks and equip our representation with the capability to capture details at different scales, we propose a hierarchical implicit subdivision strategy.

*Hierarchical Implicit Subdivision.* During optimization, base tetrahedra in  $\mathcal{M}$  identified for refinement undergo 1-to-4 subdivision, initiating the formation of a tree hierarchy. For each subdivided tetrahedron, the split is achieved by introducing a new, optimizable control point conceptually located within it. The position of this control point is parameterized by its barycentric coordinates relative to its respective parent tetrahedron. These coordinates are optimized during training, ensuring the control point remains within the parent’s volume while allowing for adaptive shaping of the resulting child tetrahedra. This subdivision process can be applied recursively if multiple levels of detail are desired, further extending this hierarchical structure.

This hierarchical structure fulfills a crucial dual role in our representation. The root nodes of this tree consistently form the conformal mesh  $\mathcal{M}$  designated for physical simulation, preserving its fixed topology and structural integrity. Conversely, the leaf tetrahedra of this tree hierarchy, representing the finest level of adaptive detail, constitute the mesh  $\mathcal{M}_r$ , utilized for high-fidelity rendering.

### 3.3 Inversion-free Structured Geometry

One of our goals is to optimize the base mesh  $\mathcal{M}$  while maintaining high-quality structure. As shown in Fig. 6 (W/o constraints), optimizing a tetrahedral mesh without any constraints leads to poor mesh quality. The main cause of this issue is that the vertices can freely move during the optimization of the tetrahedral mesh.

Consequently, the tetrahedral mesh suffers from self-intersections and element inversion problems, resulting in tetrahedra overlaps as shown in Fig. 5.

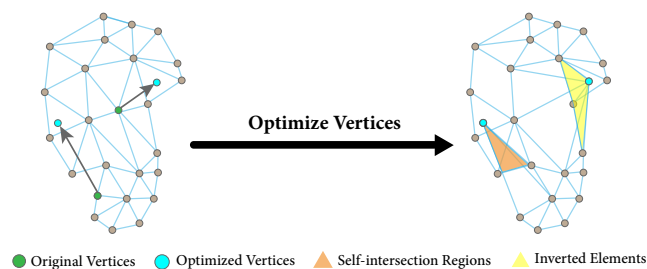


Fig. 5. **Two causes leading to mesh anomalies: self intersection and element inversion.**

A naive solution is to introduce a loss function to constrain the mesh optimization process. Locally injective mapping [Schüller et al. 2013] uses a barrier function to strictly prevent element inversion. However, the gradient explosion near the critical points of the barrier function makes it difficult to use directly in gradient descent-based optimization. Another approach is to apply an  $L_1$ -norm constraint on the signed volume of the optimized tetrahedra  $\mathcal{L}_{sv}$ , making tetrahedra with negative signed volume sparse:

$$\mathcal{L}_{sv} = \frac{1}{K} \sum_{k=1}^K \max(-s(T_k), 0), \quad (5)$$

where  $s(T_k)$  is the signed volume of the tetrahedron  $T_k$ ,  $T_k^0$  is the initial tetrahedron. However, we found that these loss function-based constraints significantly impact the rendering quality and do not fully guarantee that the tetrahedral mesh remains a reasonable structure as shown in Sec. 4.1.

*Orientation-preserving Homeomorphism as constraint.* Unlike previous methods that used regularization loss, we adopt the orientation-preserving homeomorphism as a constraint, implicitly restricting the feasible region of the vertex set  $\mathcal{V}$  of the tetrahedral mesh. The two key properties of this mapping are:

- **Orientation-preserving** means that the Jacobian determinant of the mapping remains positive, which prevents element inversion during tetrahedral mesh optimization.

- **Homeomorphism** guarantees that the tetrahedral mesh after optimization does not produce self-intersecting boundaries.

During optimization, both the topology  $\mathcal{T}$  and vertex positions  $\mathcal{V}$  of the base mesh  $\mathcal{M}$  are fixed. The orientation-preserving homeomorphism maps a vertex  $v = [x, y, z]$  to its actual position as follows:

$$v' = [x', y', z']^T = \mathcal{H}([x, y, z]^T). \quad (6)$$

We use the mapped vertices  $\mathcal{V}' = \{v'_i\}$  to reparameterize the 3D Gaussians. This orientation-preserving homeomorphism can be viewed as a constraint on the feasible region of the vertices, ensuring that a valid mesh is still generated given a topology  $\mathcal{T}$ .

*Real-NVP.* Based on these observations, we implement the orientation-preserving homeomorphism  $\mathcal{H}$  by a novel invertible network. Real-NVP [Dinh et al. 2017] appears to be a reasonable network architecture, as it is bijective and ensures that the Jacobian determinant of each coupling layer remains positive. Real-NVP splits the input  $x \in \mathbb{R}^D$  into two components,  $x_{1:d}$  and  $x_{d+1:D}$ . The output of a coupling layer  $x' \in \mathbb{R}^D$  follows the equations:

$$x'_{1:d} = x_{1:d}, \quad x'_{d+1:D} = x_{d+1:D} \cdot \exp(s(x_{1:d})) + t(x_{1:d}), \quad (7)$$

where  $s : \mathbb{R}^d \rightarrow \mathbb{R}_+^{D-d}$  and  $t : \mathbb{R}^d \rightarrow \mathbb{R}^{D-d}$  are the scale and translation functions. We denote this map of the coupling layer as  $h : \mathbb{R}^D \rightarrow \mathbb{R}^D$ . The Jacobian of this mapping is:

$$J_h = \begin{bmatrix} I & 0 \\ \frac{\partial x'_{d+1:D}}{\partial x_{1:d}} & \text{diag}[\exp(s(x_{1:d}))] \end{bmatrix}. \quad (8)$$

This is a lower triangular matrix, so its determinant is the product of the diagonal elements, which is positive. Real-NVP stacks multiple coupling layers in an alternating pattern, such that the components that are left unchanged in one coupling layer are updated in the next coupling layer. However, when we split  $(x, y, z)$  into two components:  $(x, z)$  and  $y$ , after mapping by a similar coupling layer, the Jacobian matrix is in the following form, which is not a triangular matrix, and its determinant does not remain positive.

$$J_h = \begin{bmatrix} 1 & \frac{\partial y'}{\partial x} & 0 \\ 0 & \exp(s) & 0 \\ 0 & \frac{\partial y'}{\partial z} & 1 \end{bmatrix} \quad (9)$$

*Orientation-preserving Networks.* The above problem is caused by the fact that the input is split into discontinuous parts, resulting in the Jacobian matrix being neither an upper triangular matrix nor a lower triangular matrix. To solve this problem, we propose a permutation strategy. As shown in Fig. 4, we multiply the input by a permutation matrix  $P$ , ensuring that the input is always divided into contiguous two parts. For example, when we need to keep the  $x$  and  $z$  components unchanged and transform the  $y$  component, we apply the permutation matrix  $P$  to the input and output. Therefore, the permuted transformation mapping  $\phi : \mathbb{R}^3 \rightarrow \mathbb{R}^3$  is:

$$\phi([x, y, z]^T) = P^{-1} \left( h \left( P[x, y, z]^T \right) \right), \quad P = \begin{bmatrix} 0 & 0 & 1 \\ 1 & 0 & 0 \\ 0 & 1 & 0 \end{bmatrix}. \quad (10)$$

Thus, the Jacobian matrix is:  $J_\phi = PJ_hP^{-1}$ , where  $J_h$  is the Jacobian matrix of the coupling layer  $h$ . Since  $J_h$  is an upper triangular matrix, and its diagonal elements are positive, it satisfies  $\det(J_h) > 0$ . As  $\det(P) > 0$ , it follows that  $\det(J_\phi) > 0$ .

### 3.4 Training

*Initialization.* We use two different initialization strategies. In the first strategy, we reconstruct the surface using NeuS2 [Wang et al. 2023a], and then generate the tetrahedral mesh from the reconstructed triangle mesh using fTetWild [Hu et al. 2020]. The second is to generate a uniform tetrahedral grid within the bounding box of the scene. We conduct experiments on different initialization strategies in Sec. 4.1, which show that even with poorly initialized tetrahedral mesh, we can still achieve high-quality rendering results.

*Adaptive Control of Primitives.* As detailed in Sec. 3.2, our primary mechanism for adapting geometric detail for rendering is the hierarchical implicit subdivision strategy. This approach inherently avoids direct modification of the base mesh  $\mathcal{M}$  topology. To manage the set of active rendering primitives in  $\mathcal{M}_r$  during optimization, we introduce an adaptive masking mechanism. Specifically, rendering tetrahedra whose opacity  $o_k$  falls below a predefined threshold  $\epsilon$  are masked. These masked tetrahedra no longer contribute to the rendering process. This strategy contrasts with directly deleting tetrahedra from the fixed-topology base mesh, which could introduce problematic structural changes or compromise conformality.

*Optimization.* Our model is trained by minimizing a composite loss function:

$$\mathcal{L} = \mathcal{L}_{render} + \lambda_3 \mathcal{L}_{mask} + \lambda_4 \mathcal{L}_{quality}. \quad (11)$$

The loss used for supervision of the RGB signal:  $\mathcal{L}_{render} = \lambda_1 \mathcal{L}_1 + \lambda_2 \mathcal{L}_{SSIM}$  follow 3D Gaussian splatting [Kerbl et al. 2023].  $\mathcal{L}_{mask}$  is designed to prevent artifacts at the object boundaries:

$$\mathcal{L}_{mask} = \|M - \hat{M}\|_1,$$

where  $M$  represents the rendered opacity, and  $\hat{M}$  represents the ground truth opacity.

To specifically enhance the geometric quality of the base tetrahedral mesh, we introduce  $\mathcal{L}_{quality}$  [Lo 1997]:

$$\mathcal{L}_{quality} = \frac{1}{K} \sum_{k=1}^K \max(r - Q, 0), \quad Q = \frac{C_0 V}{S_{rms}}, \quad (12)$$

where  $V$  represents the tetrahedron's volume,  $C_0$  is a normalization constant to ensure  $Q = 1$  for an equilateral tetrahedron, and  $S_{rms}$  denotes the root-mean-square of the six edge lengths of the tetrahedron. This loss essentially constrains the quality of the tetrahedron to be greater than  $r$ .

## 4 Experiments

We first give the implementation details. The contribution analysis of proposed components is given in Sec. 4.1. Evaluations of our proposed representation with previous state-of-the-art non-editable and editable approaches are presented in Sec. 4.2. We also show some applications of our proposed representation in Sec. 4.3.

Table 1. **Quantitative results with different constraints.** Mesh quality is measured by the Aspect Ratio Gamma.

	Rendering Quality			Mesh Quality	
	PSNR $\uparrow$	SSIM $\uparrow$	LPIPS $\downarrow$	Quality $\uparrow$	# Inverted $\downarrow$
(a) W/o Constraints	34.89	0.978	0.0210	$0.159 \pm 0.179$	$\sim 83.2k$
(b) W/ $\mathcal{L}_{sv}$	33.59	0.975	0.0294	$0.144 \pm 0.187$	$\sim 53.6k$
(c) W/ $\mathcal{H}$	34.64	0.974	0.0220	$0.471 \pm 0.259$	$\sim 1.3k$
(d) W/ $\mathcal{H} + \mathcal{L}_{quality}$	33.64	0.974	0.0455	$0.816 \pm 0.058$	0
(e) W/o Optimization	32.78	0.971	0.0545	$0.797 \pm 0.111$	0

*Implementation Details.* We set  $\lambda_1 = 0.8$ ,  $\lambda_2 = 0.2$ ,  $\lambda_3 = 0.5$ , and  $\lambda_4 = 10.0$  for training the model. We use the ReLU function to prevent the weights of the vertices from being negative, and apply the sigmoid function to ensure that the opacity stays within the range of  $[0, 1)$ . The gradient threshold  $\delta$  for tetrahedron splitting is set to 0.0002, the same value used in 3DGS. We set the pruning threshold  $\epsilon = 0.05$  to mask low-opacity tetrahedra. The invertible neural network consists of 3 blocks, with each axis chosen in order. A 2D hash encoding is used with a size of  $2^{19}$  and a maximum resolution of  $1024^2$ . The MLP has 2 hidden layers, each with 128 units. Additionally, we reconstruct the surface with NeuS2 [Wang et al. 2023a] and generate the initial tetrahedral mesh through fTetWild [Hu et al. 2020]. Furthermore, we limit the maximum subdivision depth for each tetrahedron to 5 levels. We train each model with 30,000 iterations, which takes approximately 1 hour. All experiments are conducted on a single NVIDIA RTX4090 GPU.

#### 4.1 Ablation Study

In this section, we conduct two main ablation studies to address the following questions:

- Q1: How much does our orientation-preserving homeomorphism and  $\mathcal{L}_{quality}$  affect rendering quality and mesh quality?
- Q2: Does an initially low-quality mesh degrade our reconstruction quality?

*Q1: Effect of Orientation-preserving Homeomorphism and  $\mathcal{L}_{quality}$ .* We conduct this experiment on the *Lego* and *Chair* scenes of *NeRF synthetic* dataset, with the mesh initialized by NeuS2 as input. To avoid the influence of number of primitives on the experiment, we remove the module of adaptive control of primitives, fixing the number of tetrahedra. We regularize the training of the tetrahedral mesh using four different methods: (a) without explicit constraints, (b) with the signed volume loss  $\mathcal{L}_{sv}$ , (c) with our orientation-preserving homeomorphism  $\mathcal{H}$  as a constraint, and (d) with both  $\mathcal{H}$  and our mesh quality loss  $\mathcal{L}_{quality}$  applied together. Furthermore, we provide a (e) baseline where the tetrahedral mesh vertices are not optimized, and only other rendering attributes are refined.

Tab. 1 and Fig. 6 present a comparison of reconstruction quality and geometric quality for these methods. Optimizing the mesh directly (without constraints) and optimizing with our homeomorphism  $\mathcal{H}$  achieve comparable rendering quality. However, employing our  $\mathcal{H}$  results in significantly fewer inverted elements and higher overall geometric quality. In contrast, applying the  $\mathcal{L}_{sv}$  loss has a limited effect on reducing the number of inverted elements and

Table 2. **Quantitative results for different initializations.**

	<i>lego</i>		<i>hotdog</i>		<i>mic</i>	
	PSNR $\uparrow$	SSIM $\uparrow$	PSNR $\uparrow$	SSIM $\uparrow$	PSNR $\uparrow$	SSIM $\uparrow$
W/o Rotation	33.27	0.968	36.14	0.975	36.06	0.986
W/ Uniform	34.98	0.980	36.90	0.983	37.46	0.991
W/ NeuS2	35.50	0.983	37.80	0.986	37.64	0.993

noticeably degrades rendering quality. This suggests that our approach of defining the feasible optimization space for vertices via an orientation-preserving homeomorphism is less susceptible to converging to poor local minima compared to methods based solely on regularization penalties. The geometric quality regularization term  $\mathcal{L}_{quality}$  leads to a slight decrease in rendering quality compared to using  $\mathcal{H}$  alone, but it yields a substantial improvement in the geometric quality of the mesh elements.

We present more visual results of the optimized mesh in Fig. 12 and numerical results in Tab. 5 and Tab. 5. The reported mesh quality metrics include AR (Aspect Ratio), defined as  $3r_k/\rho_k$  (where  $r_k$  is the inradius, and  $\rho_k$  is the circumradius of tetrahedron  $T_k$ ). ARG (Aspect Ratio Gamma) is consistent with the quality metric  $Q$  in Eq. 12. Lastly, AVR (Adjacent cells Volume Ratio) measures the ratio of the largest to smallest cell volume within the 1-ring neighborhood of a tetrahedron. Notably, after constrain with our orientation-preserving homeomorphism  $\mathcal{H}$  and  $\mathcal{L}_{quality}$  term, the geometric quality of our final mesh often surpasses that of the initial mesh.

*Q2: Ablations on Initial Mesh.* We conduct this experiment on the *NeRF synthetic* dataset: *lego*, *hotdog*, *mic*. Initially, we start with a uniform tetrahedral mesh as described in Sec. 3.4. This tetrahedral mesh is then used as input into our method for training. Tab. 2 shows the final reconstruction results under different settings compared to those obtained with NeuS2 initialization. Notably, “W/o Rotation” means the removal of the optimizable rotation parameters in Eq. 3, which leads to a significant degradation in reconstruction quality. This performance drop is likely because the per-vertex weights are then solely responsible for determining both the shape and effective orientation of the 3D Gaussians, thereby limiting their expressive ability. Conversely, when the optimizable rotation parameters are included, the “W/ Uniform” initialization setting still produces reconstruction results comparable to those achieved with the NeuS2 initialization (“W/ NeuS2”).

#### 4.2 Comparison

We conduct experiments to compare the performance of rendering on static scenes. The results show that, despite the need to maintain a structured geometry during optimization, we are still able to achieve comparable results to that of unstructured radiance field representation like 3DGS [Kerbl et al. 2023].

We employ two datasets for evaluation: *NeRF Synthetic* dataset [Mildenhall et al. 2020a], containing eight scenes and *Shelly* dataset [Wang et al. 2023b], containing six scenes. We conduct comparisons with implicit, point-based, and mesh-based methods to evaluate the performance of our approach, including NeRF [Mildenhall et al. 2020a],

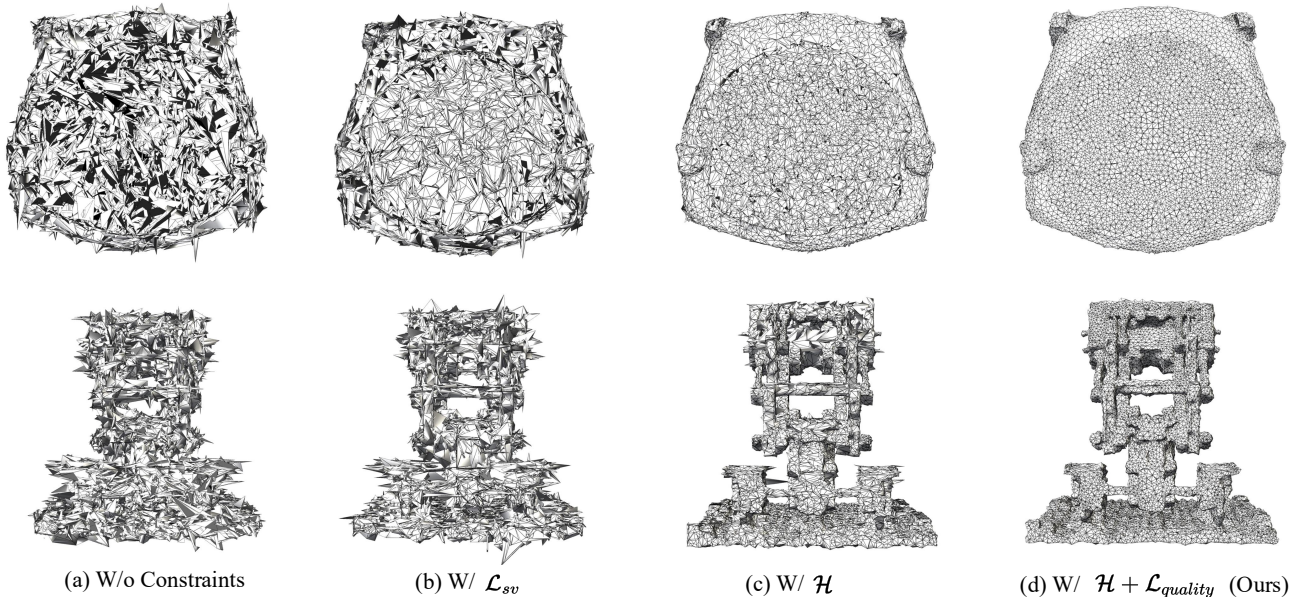


Fig. 6. Visualization of tetrahedral mesh cross-sections optimized with different constraints.

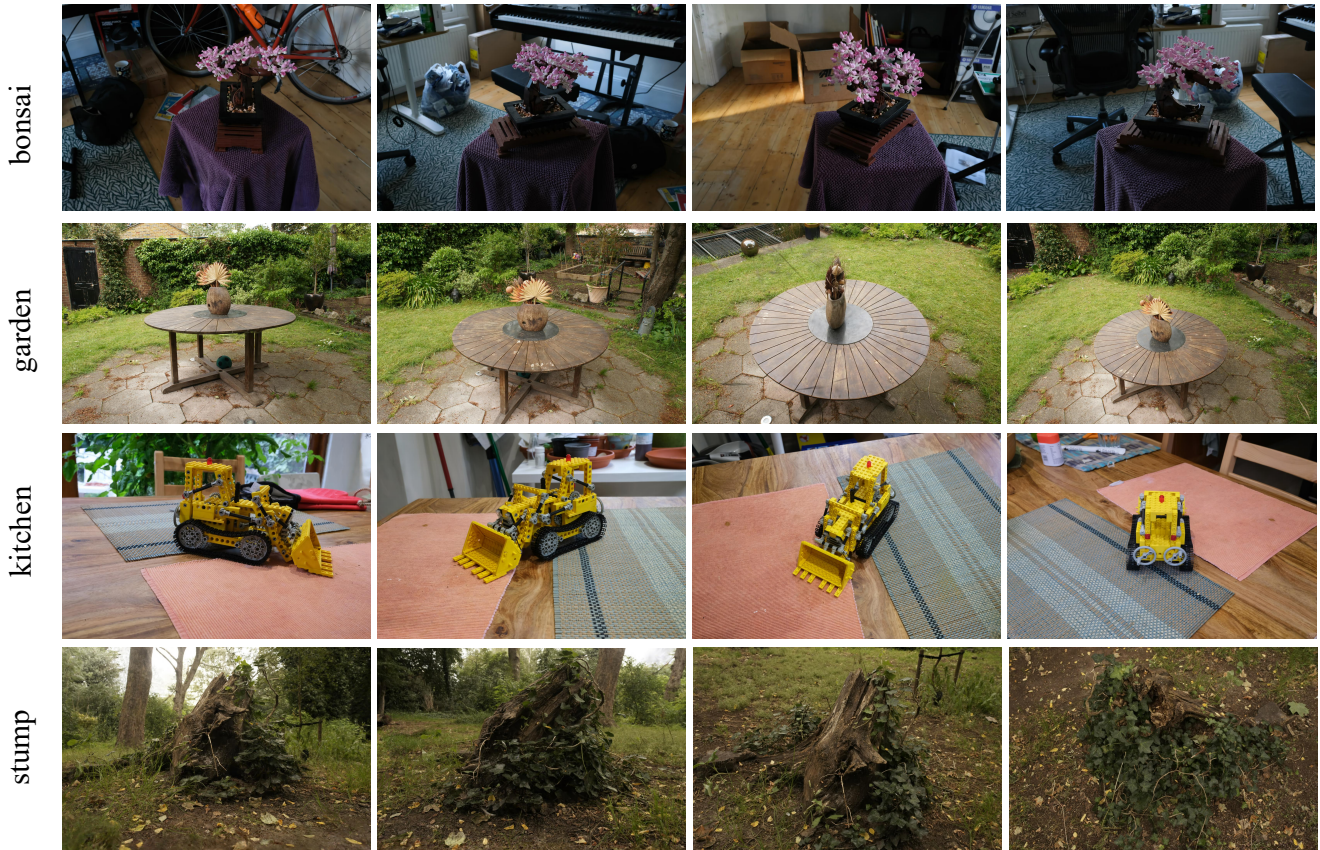


Fig. 7. Gallery of Rendering Results on *MipNeRF 360* dataset.

Table 3. Quantitative results on NeRF Synthetic and Shelly dataset.

	NeRF Synthetic			Shelly		
	PSNR $\uparrow$	SSIM $\uparrow$	LPIPS $\downarrow$	PSNR $\uparrow$	SSIM $\uparrow$	LPIPS $\downarrow$
NeRF	31.00	0.947	0.081	31.28	0.893	0.157
Adaptive Shells	31.84	0.957	0.056	36.02	0.954	0.079
3DGS	<b>33.78</b>	<b>0.969</b>	0.030	39.61	0.961	0.064
2DGS	32.92	0.966	0.036	34.62	0.928	0.098
Mani-GS	32.58	0.961	0.034	–	–	–
SuGaR	30.94	0.954	0.040	36.43	0.956	0.057
Ours	33.53	0.968	<b>0.019</b>	<b>39.76</b>	<b>0.967</b>	<b>0.052</b>

Table 4. Quantitative results on Mip-NeRF360 dataset. Results of other methods are borrowed from Radiant Foam’s paper.

	Outdoor Scene			Indoor Scene		
	PSNR $\uparrow$	SSIM $\uparrow$	LPIPS $\downarrow$	PSNR $\uparrow$	SSIM $\uparrow$	LPIPS $\downarrow$
3DGS	26.40	0.807	0.197	30.38	0.920	0.220
Mip-Splatting	<b>26.81</b>	<b>0.817</b>	<b>0.170</b>	31.19	<b>0.933</b>	0.223
MipNeRF360	25.92	0.747	0.243	<b>31.72</b>	0.915	0.180
Radiant Foam	25.42	0.737	0.253	30.75	0.908	<b>0.170</b>
Ours	25.71	0.774	0.193	30.83	0.921	0.197

3DGS [Kerbl et al. 2023], 2DGS [Huang et al. 2024b], Adaptive Shells [Wang et al. 2023b] and Mani-GS [Gao et al. 2024]. We use the surface reconstructed by NeuS2 as input to Mani-GS for a fair comparison. We use the same training process as 3DGS. The rendering quality is evaluated using a set of established metrics: PSNR, SSIM [Wang et al. 2004], and LPIPS [Zhang et al. 2018]. In Tab. 3, we conduct a quantitative comparison of rendering quality. Our approach shows competitive results across all mesh-based and point-based methods according to three evaluation metrics. Moreover, our approach achieves qualitatively better reconstructions, with fewer artifacts and more detailed results, as shown in Fig. 8.

Furthermore, to demonstrate the effectiveness of our method in real-world unbounded scenes, we conducted experiments on the MipNeRF 360 dataset [Barron et al. 2022]. For initialization in these scenes, we utilize a mesh of the centrally located region, initially reconstructed by Gaussian Opacity Fields [Yu et al. 2024]. This mesh is then tetrahedralized using fTetWild [Hu et al. 2020] to serve as the input tetrahedral mesh for our method. Our StructuredField representation is employed to reconstruct this central region of interest, while the surrounding background is modeled using standard 3D Gaussian Splatting [Kerbl et al. 2023]. Tab. 4 presents a numerical comparison of our method against several state-of-the-art approaches, including 3DGS [Kerbl et al. 2023], Mip-Splatting [Yu et al. 2004], MipNeRF360 [Barron et al. 2022], and RadiantFoam [Govindarajan et al. 2025]. Our method achieves reconstruction results comparable to those of 3DGS and surpasses RadiantFoam, another approach that also utilizes a deformable tetrahedral grid as its geometric primitive for scene representation. Additional visual results from our method on these scenes are provided in Fig. 7.

### 4.3 Applications

Our method directly constructs an explicit tetrahedral mesh  $\mathcal{M}$  with good quality and achieves good rendering quality at the same time, which proves highly valuable for a variety of downstream applications. With tetrahedral mesh, we can perform physics simulations, animations, editing, and other operations seamlessly. With our proposed StructuredField, we can easily update the mesh by simply tracking the movement or displacement of each vertex. This allows us to reparameterize the Gaussians based on the new positions of vertices, enabling the rendering of deformed scenes.

Methods like Mani-GS and GaMeS are hybrid representations that fix mesh vertex positions and establish a relationship between triangle meshes and 3D Gaussians. In contrast, our method offers a unified, structured representation where the vertex positions are optimized during the reconstruction process. Since the final meshes produced by our method differ from those in hybrid methods, it is difficult to establish a fair comparison under the same deformation.

For many applications such as physical simulation and deformation, the tetrahedral mesh representation in our StructuredField has inherent advantages. Unlike triangle meshes, which only represent the surface of an object, tetrahedral meshes have an internal structure, making it more suitable for physically accurate simulations. On the other hand, thanks to our carefully designed reparameterization strategy, the primitives in our representation are always confined within the corresponding tetrahedra. This ensures that our representation accurately reflects the mesh deformation. In contrast, previous methods using triangle meshes may suffer from artifacts during deformation, as the 3D Gaussians could shift away from the triangular surfaces, leading to potential inconsistencies between 3D Gaussians and triangle meshes.

*Physical Simulation.* After constructing the base tetrahedral mesh  $\mathcal{M}$ , we use it for physical simulation. This process yields a sequence of vertex positions defining its dynamic state over time, denoted as  $\mathcal{M}^k$ . The motion of any implicitly defined child tetrahedra is then consistently derived from their parent elements within  $\mathcal{M}^k$ . This is achieved by applying the previously optimized barycentric coordinates of the subdivision control points to the vertices of the dynamically deformed parent tetrahedra. This process yields the dynamic rendering mesh,  $\mathcal{M}_r^k$ .

To simulate elastic deformations specifically, we treat the base mesh  $\mathcal{M}$  as a mass-spring system. In this system, each vertex is modeled as a mass point, and the edges of the tetrahedra serve as springs connecting these points. We implement the XPBD algorithm [Macklin et al. 2016] using the Taichi programming language [Hu et al. 2019]. Other types of simulation effects or complementary demonstrations presented are realized in Houdini [SideFX Software Inc. 2023]. Fig. 10 shows results from our physics simulation approach; please refer to the supplementary video for dynamic motion.

*Deformation.* We utilize lattice deformation as a mechanism to drive the deformation of the tetrahedral mesh. As the mesh vertices undergo deformation, we reparameterize the associated Gaussian primitives based on the updated positions of the mesh vertices. As demonstrated in Fig. 9, even under large-scale deformations, our representation still produces reasonable rendering results.

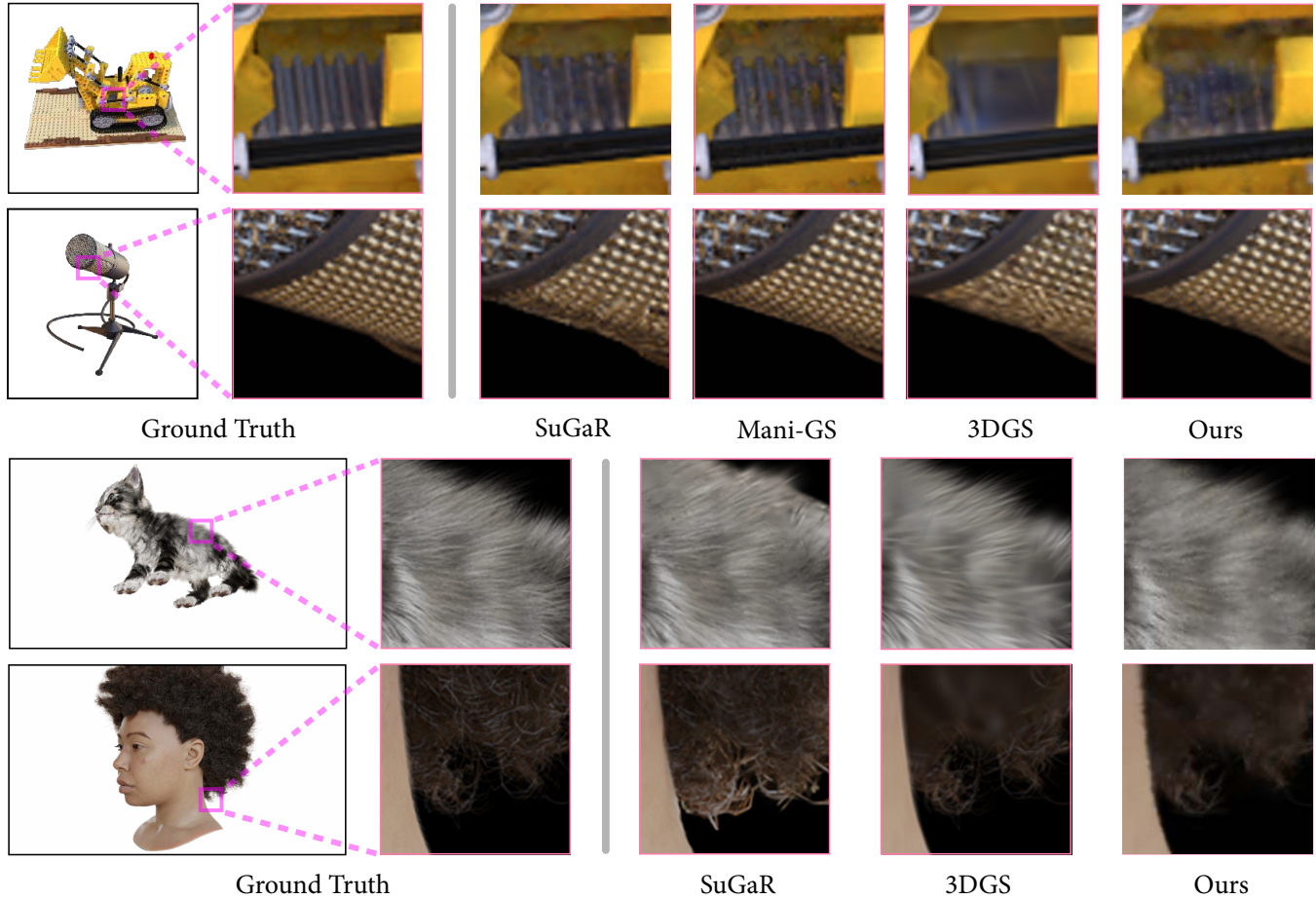


Fig. 8. Our results on the test-views of *Shelly* dataset and *NeRF Synthetic* dataset.

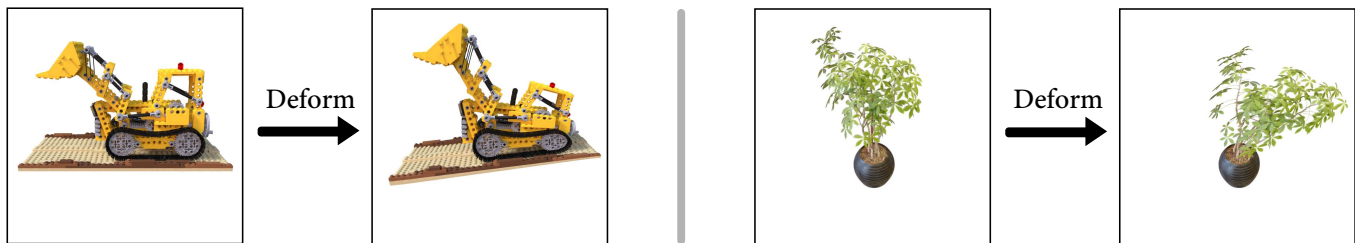


Fig. 9. Gallery of deformation results. Videos are provided in the supplementary materials for further visualization.

*Level-of-Detail.* The hierarchical nature of our implicit subdivision naturally facilitates an efficient Level of Detail (LOD) rendering strategy. This allows the complexity of the rendered scene to be dynamically adjusted, balancing visual fidelity with computational performance. Starting from the rendering mesh  $\mathcal{M}_r$ , coarser LODs are generated by progressively replacing sets of four child tetrahedra with their respective parent tetrahedron. For attributes defined per tetrahedron, the opacity of the parent tetrahedron is taken as the maximum of its four children's opacities, and its rotation quaternion

is determined by averaging the rotation quaternions of its children. Fig. 11 demonstrates the effects of our LOD approach.

## 5 Conclusion

We introduced StructuredField, a novel structured 3D representation that unifies high-fidelity rendering and structured geometry. Our main contribution is using reparameterization to make tetrahedral mesh rendering differentiable. An orientation-preserving homeomorphism has been proposed to ensure the mesh quality during

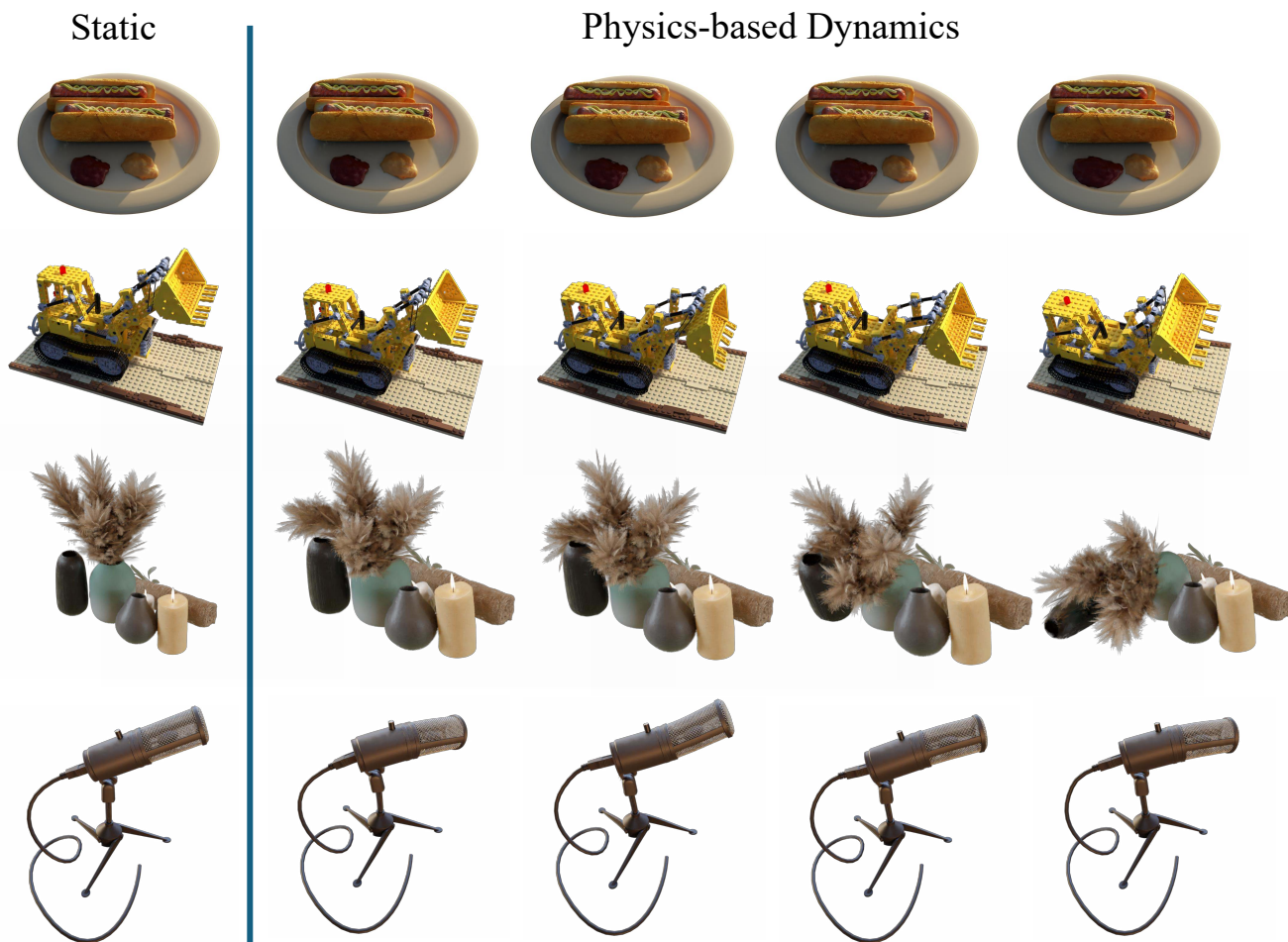


Fig. 10. **Gallery of physical simulation results.** The original shape is shown in the leftmost column, with the corresponding physical simulations displayed in the right column. Videos are provided in the supplementary materials for further visualization.

Table 5. **Quality metrics of initial mesh and optimized mesh on *NeRFSynthetic* Dataset.**

	lego			mic			ship			chair		
	AR $\uparrow$	ARG $\uparrow$	AVR $\downarrow$	AR $\uparrow$	ARG $\uparrow$	AVR $\downarrow$	AR $\uparrow$	ARG $\uparrow$	AVR $\downarrow$	AR $\uparrow$	ARG $\uparrow$	AVR $\downarrow$
Initial Mesh	0.853 $\pm$ 0.086	0.829 $\pm$ 0.091	1.234 $\pm$ 0.228	0.826 $\pm$ 0.105	0.800 $\pm$ 0.109	1.274 $\pm$ 0.297	0.823 $\pm$ 0.118	0.798 $\pm$ 0.121	1.306 $\pm$ 0.358	0.848 $\pm$ 0.097	0.824 $\pm$ 0.101	1.255 $\pm$ 0.285
Ours Mesh	<b>0.855 <math>\pm</math> 0.053</b>	<b>0.829 <math>\pm</math> 0.056</b>	<b>1.229 <math>\pm</math> 0.202</b>	<b>0.849 <math>\pm</math> 0.051</b>	<b>0.821 <math>\pm</math> 0.054</b>	<b>1.236 <math>\pm</math> 0.208</b>	<b>0.849 <math>\pm</math> 0.054</b>	<b>0.822 <math>\pm</math> 0.056</b>	<b>1.254 <math>\pm</math> 0.226</b>	<b>0.854 <math>\pm</math> 0.053</b>	<b>0.827 <math>\pm</math> 0.056</b>	<b>1.238 <math>\pm</math> 0.213</b>

optimization. Extensive experiments have been conducted to verify the effectiveness of StructuredField in the aspects of rendering quality, physics simulations, and deformation modeling.

*Limitations.* Although our proposed StructuredField representation can simultaneously recover high-quality rendering and structured geometry from multi-view images, there are still some limitations: First, during the training process, vertices need to pass through the neural network, which leads to a longer training time than unstructured radiance field representations. In addition, since

we need to maintain structured geometry during the reconstruction process, our solution space is more restricted than unstructured radiance field representations, so a larger number of primitives are required to represent the scene to achieve similar rendering effects.

#### Acknowledgments

This research was supported by the National Natural Science Foundation of China (No.62122071, No.62272433), the Youth Innovation

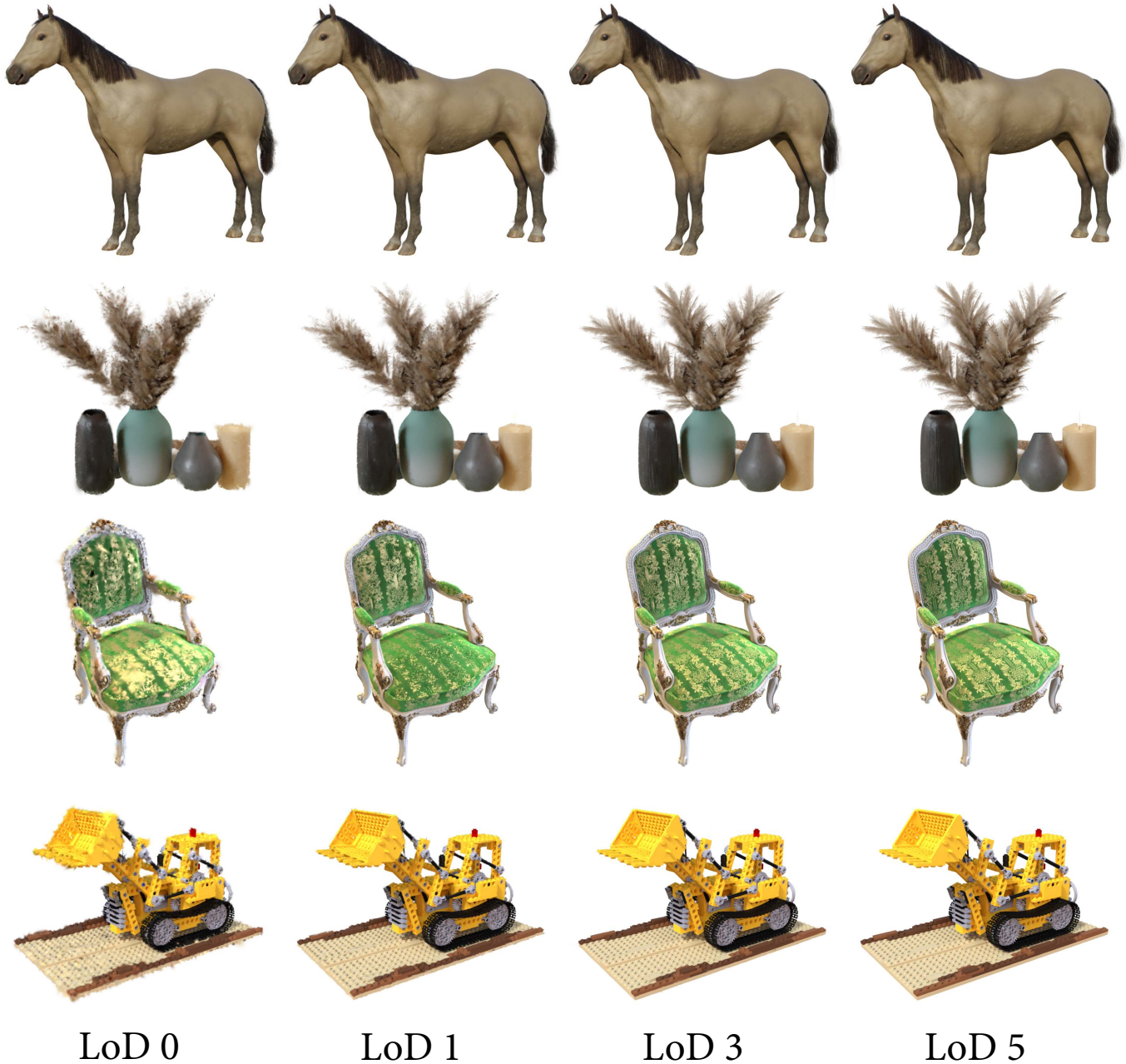


Fig. 11. Demonstration of our method’s LoD capabilities on *Shelly Dataset* and *NeRF Synthetic Dataset*.

Promotion Association CAS (No. 2018495) and the Fundamental Research Funds for the Central Universities (No. WK3470000021).

## References

- Hervé Abdi and Lynne J Williams. 2010. Principal component analysis. *Wiley interdisciplinary reviews: computational statistics* 2, 4 (2010), 433–459.
- Sameer Agarwal, Noah Snavely, Ian Simon, Steven M. Seitz, and Richard Szeliski. 2009. Building Rome in a day. In *2009 IEEE 12th International Conference on Computer Vision*. 72–79. <https://doi.org/10.1109/ICCV.2009.5459148>
- Ryoichi Ando, Nils Thürey, and Chris Wojtan. 2013. Highly adaptive liquid simulations on tetrahedral meshes. *ACM Transactions on Graphics (TOG)* 32, 4 (2013), 1–10.
- David Baraff and Andrew Witkin. 2023. Large steps in cloth simulation. In *Seminal Graphics Papers: Pushing the Boundaries, Volume 2*. 767–778.
- Jonathan T Barron, Ben Mildenhall, Matthew Tancik, Peter Hedman, Ricardo Martin-Brualla, and Pratul P Srinivasan. 2021. Mip-nerf: A multiscale representation for anti-aliasing neural radiance fields. In *Proceedings of the IEEE/CVF international conference on computer vision*. 5855–5864.
- Jonathan T Barron, Ben Mildenhall, Dor Verbin, Pratul P Srinivasan, and Peter Hedman. 2022. Mip-nerf 360: Unbounded anti-aliased neural radiance fields. In *Proceedings of the IEEE/CVF conference on computer vision and pattern recognition*. 5470–5479.

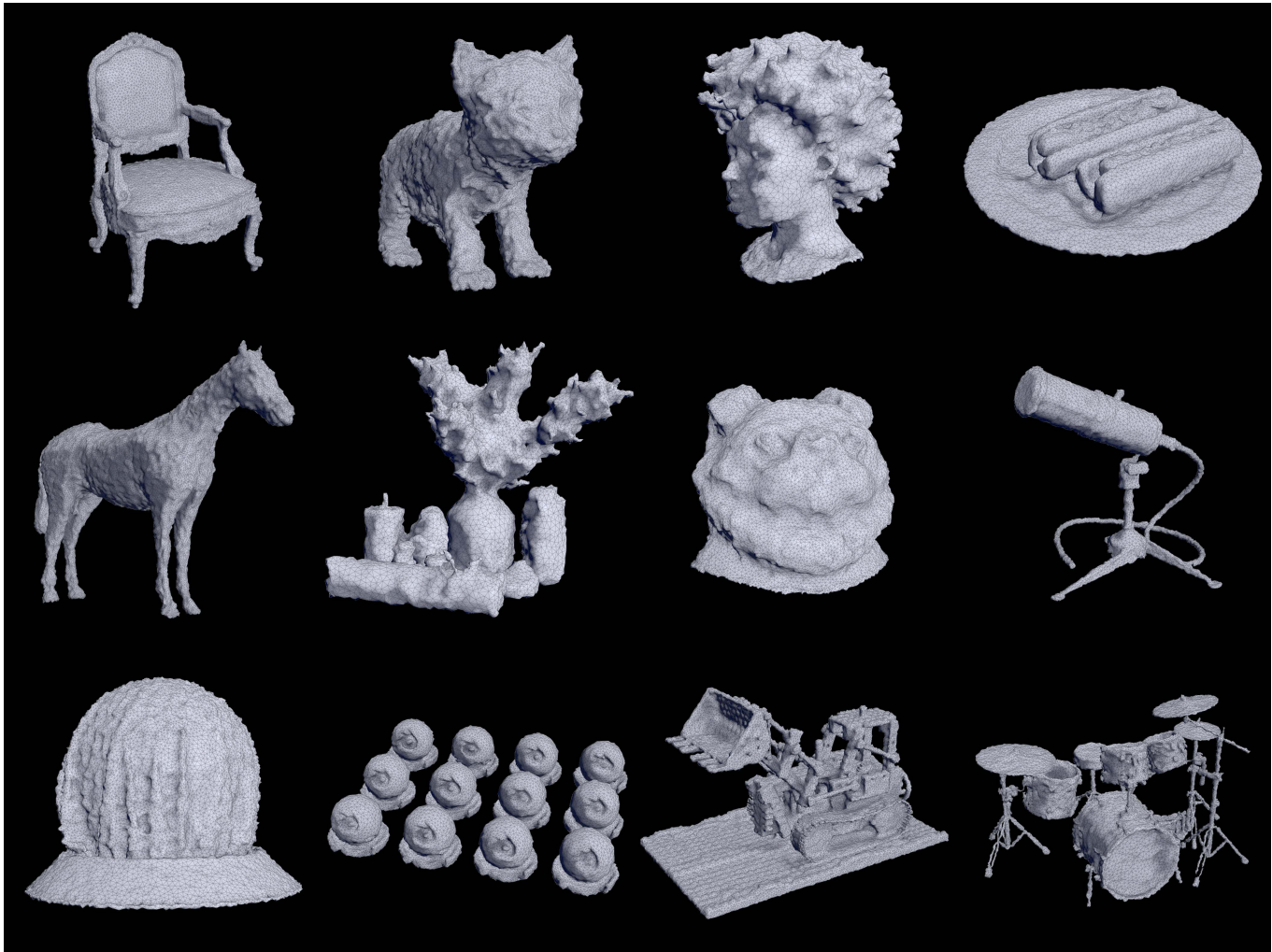


Fig. 12. Gallery of mesh results on *Shelly* dataset and *NeRF Synthetic* dataset.

- Jonathan T Barron, Ben Mildenhall, Dor Verbin, Pratul P Srinivasan, and Peter Hedman. 2023. Zip-nerf: Anti-aliased grid-based neural radiance fields. In *Proceedings of the IEEE/CVF International Conference on Computer Vision*. 19697–19705.
- Jens Behrmann, Will Grathwohl, Ricky TQ Chen, David Duvenaud, and Jörn-Henrik Jacobsen. 2019. Invertible residual networks. In *International conference on machine learning*. PMLR, 573–582.
- Mario Botsch, Alexander Hornung, Matthias Zwicker, and Leif Kobbelt. 2005. High-Quality Surface Splatting on Today's GPUs. In *2nd Symposium on Point Based Graphics, PBG 2005, Stony Brook, NY, USA, June 21-22, 2005*. 17–24.
- Hongrui Cai, Wanquan Feng, Xuetao Feng, Yan Wang, and Juyong Zhang. 2022. Neural surface reconstruction of dynamic scenes with monocular rgb-d camera. *Advances in Neural Information Processing Systems* 35 (2022), 967–981.
- Anpei Chen, Zexiang Xu, Andreas Geiger, Jingyi Yu, and Hao Su. 2022. Tensorf: Tensorial radiance fields. In *European conference on computer vision*. Springer, 333–350.
- Laurent Dinh, Jascha Sohl-Dickstein, and Samy Bengio. 2017. Density estimation using Real NVP. In *International Conference on Learning Representations (ICLR)*.
- Jan-Michael Frahm, Pierre Fite-Georgel, David Gallup, Tim Johnson, Rahul Raguram, Changchang Wu, Yi-Hung Jen, Enrique Dunn, Brian Clipp, Svetlana Lazebnik, and Marc Pollefeys. 2010. Building Rome on a cloudless day. In *Proceedings of the 11th European Conference on Computer Vision: Part IV (Heraklion, Crete, Greece) (ECCV'10)*. Springer-Verlag, Berlin, Heidelberg, 368–381.
- Xiao-Ming Fu, Jian-Ping Su, Zheng-Yu Zhao, Qing Fang, Chunyang Ye, and Ligang Liu. 2021. Inversion-free geometric mapping construction: A survey. *Computational Visual Media* 7 (2021), 289–318.
- Yasutaka Furukawa, Brian Curless, Steven M. Seitz, and Richard Szeliski. 2010. Towards Internet-scale multi-view stereo. In *2010 IEEE Computer Society Conference on Computer Vision and Pattern Recognition*. 1434–1441. <https://doi.org/10.1109/CVPR.2010.5539802>
- Yasutaka Furukawa and Jean Ponce. 2010. Accurate, Dense, and Robust Multiview Stereopsis. *IEEE Transactions on Pattern Analysis and Machine Intelligence* 32, 8 (2010), 1362–1376. <https://doi.org/10.1109/TPAMI.2009.161>
- Xiangjun Gao, Xiaoyu Li, Yiyu Zhuang, Qi Zhang, Wenbo Hu, Chaopeng Zhang, Yao Yao, Ying Shan, and Long Qian. 2024. Mani-GS: Gaussian Splatting Manipulation with Triangular Mesh. *arXiv preprint arXiv:2405.17811* (2024).
- Shrisudhan Govindarajan, Daniel Rebain, Kwang Moo Yi, and Andrea Tagliasacchi. 2025. Radiant Foam: Real-Time Differentiable Ray Tracing. *arXiv preprint arXiv:2502.01157* (2025).
- Jan Held, Renaud Vandeghen, Abdullah Hamdi, Adrien Deliege, Anthony Cioppa, Silvio Giancola, Andrea Vedaldi, Bernard Ghanem, and Marc Van Droogenbroeck. 2024. 3D Convex Splatting: Radiance Field Rendering with 3D Smooth Convexes. *arXiv preprint arXiv:2411.14974* (2024).
- Hugues Hoppe. 2023. Progressive meshes. In *Seminal Graphics Papers: Pushing the Boundaries, Volume 2*. 111–120.
- Yuanming Hu, Tzu-Mao Li, Luke Anderson, Jonathan Ragan-Kelley, and Frédo Durand. 2019. Taichi: a language for high-performance computation on spatially sparse data structures. *ACM Trans. Graph.* 38, 6, Article 201 (nov 2019), 16 pages. <https://doi.org/10.1145/3355089.3356506>

- Yixin Hu, Teseo Schneider, Bolun Wang, Denis Zorin, and Daniele Panozzo. 2020. Fast tetrahedral meshing in the wild. *ACM Transactions on Graphics (TOG)* 39, 4 (2020), 117–1.
- Binbin Huang, Zehao Yu, Anpei Chen, Andreas Geiger, and Shenghua Gao. 2024b. 2D Gaussian Splatting for Geometrically Accurate Radiance Fields. In *SIGGRAPH 2024 Conference Papers*. Association for Computing Machinery. <https://doi.org/10.1145/3641519.3657428>
- Yi-Hua Huang, Ming-Xian Lin, Yang-Tian Sun, Ziyi Yang, Xiaoyang Lyu, Yan-Pei Cao, and Xiaojuan Qi. 2024a. Deformable Radial Kernel Splatting. *arXiv preprint arXiv:2412.11752* (2024).
- Clément Jambon, Bernhard Kerbl, Georgios Kopanas, Stavros Diatzis, Thomas Leimkühler, and George Drettakis. 2023. Nerfshop: Interactive editing of neural radiance fields. *Proceedings of the ACM on Computer Graphics and Interactive Techniques* 6, 1 (2023).
- Doug L James and Christopher D Twigg. 2005. Skinning mesh animations. *ACM Transactions on Graphics (TOG)* 24, 3 (2005), 399–407.
- Ying Jiang, Chang Yu, Tianyi Xie, Xuan Li, Yutao Feng, Huamin Wang, Minchen Li, Henry Lau, Feng Gao, Yin Yang, et al. 2024. Vr-gs: A physical dynamics-aware interactive gaussian splatting system in virtual reality. In *ACM SIGGRAPH 2024 Conference Papers*. 1–1.
- Zhongshi Jiang, Scott Schaefer, and Daniele Panozzo. 2017. Simplicial complex augmentation framework for bijective maps. *ACM Transactions on Graphics* 36, 6 (2017).
- Hailin Jin, Stefano Soatto, and Anthony J. Yezzi. 2005. Multi-View Stereo Reconstruction of Dense Shape and Complex Appearance. *International Journal of Computer Vision* 63 (2005), 175–189. <https://api.semanticscholar.org/CorpusID:2067330>
- Nikhil Keetha, Jay Karhade, Krishna Murthy Jatavallabhula, Gengshan Yang, Sebastian Scherer, Deva Ramanan, and Jonathan Luiten. 2024. SplatTAM: Splat Track & Map 3D Gaussians for Dense RGB-D SLAM. In *Proceedings of the IEEE/CVF Conference on Computer Vision and Pattern Recognition*. 21357–21366.
- Bernhard Kerbl, Georgios Kopanas, Thomas Leimkühler, and George Drettakis. 2023. 3D Gaussian Splatting for Real-Time Radiance Field Rendering. *ACM Transactions on Graphics* 42, 4 (July 2023). <https://repo-sam.inria.fr/fungraph/3d-gaussian-splatting/>
- Jonas Kulhanek and Torsten Sattler. 2023. Tetra-nerf: Representing neural radiance fields using tetrahedra. In *Proceedings of the IEEE/CVF International Conference on Computer Vision*. 18458–18469.
- Jiahui Lei and Kostas Daniilidis. 2022. Cadex: Learning canonical deformation coordinate space for dynamic surface representation via neural homeomorphism. In *Proceedings of the IEEE/CVF Conference on Computer Vision and Pattern Recognition*. 6624–6634.
- Jiaqi Lin, Zhihao Li, Xiao Tang, Jianzhuang Liu, Shiyong Liu, Jiayue Liu, Yangdi Lu, Xiaofei Wu, Songcen Xu, Youliang Yan, et al. 2024. Vastgaussian: Vast 3d gaussians for large scene reconstruction. In *Proceedings of the IEEE/CVF Conference on Computer Vision and Pattern Recognition*. 5166–5175.
- Shichen Liu, Tianye Li, Weikai Chen, and Hao Li. 2019. Soft rasterizer: A differentiable renderer for image-based 3d reasoning. In *Proceedings of the IEEE/CVF international conference on computer vision*. 7708–7717.
- Tiantian Liu, Adam W Bargteil, James F O'Brien, and Ladislav Kavan. 2013. Fast simulation of mass-spring systems. *ACM Transactions on Graphics (TOG)* 32, 6 (2013), 1–7.
- SH Lo. 1997. Optimization of tetrahedral meshes based on element shape measures. *Computers & structures* 63, 5 (1997), 951–961.
- Kwan-Liu Ma and Thomas W Crockett. 1997. A scalable parallel cell-projection volume rendering algorithm for three-dimensional unstructured data. In *Proceedings of the IEEE symposium on Parallel rendering*. 95–ff.
- Miles Macklin, Matthias Müller, and Nuttapon Chentanez. 2016. XPBD: position-based simulation of compliant constrained dynamics. In *Proceedings of the 9th International Conference on Motion in Games (Burlingame, California) (MIG '16)*. Association for Computing Machinery, New York, NY, USA, 49–54. <https://doi.org/10.1145/2994258.2994272>
- Ben Mildenhall, Pratul P. Srinivasan, Matthew Tancik, Jonathan T. Barron, Ravi Ramamoorthi, and Ren Ng. 2020a. NeRF: Representing Scenes as Neural Radiance Fields for View Synthesis. In *European Conference on Computer Vision (ECCV)*.
- Ben Mildenhall, Pratul P. Srinivasan, Matthew Tancik, Jonathan T. Barron, Ravi Ramamoorthi, and Ren Ng. 2020b. NeRF: Representing Scenes as Neural Radiance Fields for View Synthesis. In *ECCV*.
- Marek Krzysztow Misztal and Jakob Andreas Bærentzen. 2012. Topology-adaptive interface tracking using the deformable simplicial complex. *ACM Transactions on Graphics (TOG)* 31, 3 (2012), 1–12.
- Thomas Müller, Alex Evans, Christoph Schied, and Alexander Keller. 2022. Instant neural graphics primitives with a multiresolution hash encoding. *ACM transactions on graphics (TOG)* 41, 4 (2022), 1–15.
- Yicong Peng, Yichao Yan, Shengqi Liu, Yuhao Cheng, Shanyan Guan, Bowen Pan, Guangtao Zhai, and Xiaokang Yang. 2022. Cagenerf: Cage-based neural radiance field for generalized 3d deformation and animation. *Advances in Neural Information Processing Systems* 35 (2022), 31402–31415.
- Stanislav Pidhorskyi, Tomas Simon, Gabriel Schwartz, He Wen, Yaser Sheikh, and Jason Saragih. 2025. Rasterized Edge Gradients: Handling Discontinuities Differentiably. In *European Conference on Computer Vision*. Springer, 335–352.
- Michael Rabinovich, Roi Poranne, Daniele Panozzo, and Olga Sorkine-Hornung. 2017. Scalable locally injective mappings. *ACM Transactions on Graphics (TOG)* 36, 4 (2017), 1.
- Christian Reiser, Stephan Garbin, Pratul Srinivasan, Dor Verbin, Richard Szeliski, Ben Mildenhall, Jonathan Barron, Peter Hedman, and Andreas Geiger. 2024. Binary opacity grids: Capturing fine geometric detail for mesh-based view synthesis. *ACM Transactions on Graphics (TOG)* 43, 4 (2024), 1–14.
- Radu Alexandru Rosu and Sven Behnke. 2023. Permutosdf: Fast multi-view reconstruction with implicit surfaces using permutohedral lattices. In *Proceedings of the IEEE/CVF Conference on Computer Vision and Pattern Recognition*. 8466–8475.
- Szymon Rusinkiewicz and Marc Levoy. 2000. QSplat: A multiresolution point rendering system for large meshes. In *Proceedings of the 27th annual conference on Computer graphics and interactive techniques*. 343–352.
- Christian Schüller, Ladislav Kavan, Daniele Panozzo, and Olga Sorkine-Hornung. 2013. Locally injective mappings. In *Computer Graphics Forum*, Vol. 32. Wiley Online Library, 125–135.
- SideFX Software Inc. 2023. Houdini. <https://www.sidefx.com>
- Olga Sorkine and Marc Alexa. 2007. As-rigid-as-possible surface modeling. In *Symposium on Geometry processing*, Vol. 4. Citeseer, 109–116.
- Matthew Tancik, Vincent Casser, Xinchen Yan, Sabeek Pradhan, Ben Mildenhall, Pratul P Srinivasan, Jonathan T Barron, and Henrik Kretschmar. 2022. Block-nerf: Scalable large scene neural view synthesis. In *Proceedings of the IEEE/CVF Conference on Computer Vision and Pattern Recognition*. 8248–8258.
- Jiaxiang Tang, Jiawei Ren, Hang Zhou, Ziwei Liu, and Gang Zeng. 2024. DreamGaussian: Generative Gaussian Splatting for Efficient 3D Content Creation. In *International Conference on Learning Representations (ICLR)*.
- Haithem Turki, Vasu Agrawal, Samuel Rota Bulò, Lorenzo Porzi, Peter Kotschieder, Deva Ramanan, Michael Zollhöfer, and Christian Richardt. 2024. HybridNeRF: Efficient Neural Rendering via Adaptive Volumetric Surfaces. In *Proceedings of the IEEE/CVF Conference on Computer Vision and Pattern Recognition*. 19647–19656.
- Ziyu Wan, Christian Richardt, Aljaž Božič, Chao Li, Vijay Rengarajan, Seonghyeon Nam, Xiaoyu Xiang, Tuotuo Li, Bo Zhu, Rakesh Ranjan, et al. 2023. Learning neural duplex radiance fields for real-time view synthesis. In *Proceedings of the IEEE/CVF Conference on Computer Vision and Pattern Recognition*. 8307–8316.
- Peng Wang, Lingjie Liu, Yuan Liu, Christian Theobalt, Taku Komura, and Wenping Wang. 2021. NeuS: Learning Neural Implicit Surfaces by Volume Rendering for Multi-view Reconstruction. In *Advances in Neural Information Processing Systems 34: Annual Conference on Neural Information Processing Systems 2021, NeurIPS 2021, December 6–14, 2021, virtual*, Marc Aurelio Ranzato, Alina Beygelzimer, Yann N. Dauphin, Percy Liang, and Jennifer Wortman Vaughan (Eds.). 27171–27183.
- Yiming Wang, Qin Han, Marc Habermann, Kostas Daniilidis, Christian Theobalt, and Lingjie Liu. 2023a. NeuS2: Fast learning of neural implicit surfaces for multi-view reconstruction. In *Proceedings of the IEEE/CVF International Conference on Computer Vision*. 3295–3306.
- Zhou Wang, Alan C Bovik, Hamid R Sheikh, and Eero P Simoncelli. 2004. Image quality assessment: from error visibility to structural similarity. *IEEE transactions on image processing* 13, 4 (2004), 600–612.
- Zian Wang, Tianchang Shen, Merlin Nimier-David, Nicholas Sharp, Jun Gao, Alexander Keller, Sanja Fidler, Thomas Müller, and Zan Gojcic. 2023b. Adaptive Shells for Efficient Neural Radiance Field Rendering. *ACM Trans. Graph.* 42, 6 (2023), 260:1–260:15.
- Manfred Weiler, Martin Kraus, Markus Merz, and Thomas Ertl. 2003. Hardware-based view-independent cell projection. *IEEE Transactions on Visualization and Computer Graphics* 9, 2 (2003), 163–175.
- Mason Woo, Jackie Neider, Tom Davis, and Dave Shreiner. 1999. *OpenGL programming guide: the official guide to learning OpenGL, version 1.2*. Addison-Wesley Longman Publishing Co., Inc.
- Jun Xiang, Xuan Gao, Yudong Guo, and Juyong Zhang. 2024. FlashAvatar: High-fidelity Head Avatar with Efficient Gaussian Embedding. In *Proceedings of the IEEE/CVF Conference on Computer Vision and Pattern Recognition*. 1802–1812.
- Roni Yagel, David M Reed, Asish Law, Po-Wen Shih, and Naem Shareef. 1996. Hardware assisted volume rendering of unstructured grids by incremental slicing. In *Proceedings of 1996 Symposium on Volume Visualization*. IEEE, 55–62.
- Guandao Yang, Serge Belongie, Bharath Hariharan, and Vladlen Koltun. 2021. Geometry Processing with Neural Fields. In *Thirty-Fifth Conference on Neural Information Processing Systems*.
- Lior Yariv, Peter Hedman, Christian Reiser, Dor Verbin, Pratul P Srinivasan, Richard Szeliski, Jonathan T Barron, and Ben Mildenhall. 2023. BakedSDF: Meshing neural sdf for real-time view synthesis. In *ACM SIGGRAPH 2023 Conference Proceedings*. 1–9.
- Wang Yifan, Felice Serena, Shihao Wu, Cengiz Öztireli, and Olga Sorkine-Hornung. 2019. Differentiable surface splatting for point-based geometry processing. *ACM Transactions on Graphics (TOG)* 38, 6 (2019), 1–14.

- Yizhou Yu, Kun Zhou, Dong Xu, Xiaohan Shi, Hujun Bao, Baining Guo, and Heung-Yeung Shum. 2004. Mesh editing with poisson-based gradient field manipulation. In *ACM SIGGRAPH 2004 Papers*. 644–651.
- Zehao Yu, Torsten Sattler, and Andreas Geiger. 2024. Gaussian opacity fields: Efficient adaptive surface reconstruction in unbounded scenes. *ACM Transactions on Graphics (TOG)* 43, 6 (2024), 1–13.
- Richard Zhang, Phillip Isola, Alexei A Efros, Eli Shechtman, and Oliver Wang. 2018. The unreasonable effectiveness of deep features as a perceptual metric. In *Proceedings of the IEEE conference on computer vision and pattern recognition*. 586–595.
- Wojciech Zielonka, Timur Bagautdinov, Shunsuke Saito, Michael Zollhöfer, Justus Thies, and Javier Romero. 2025. Drivable 3D Gaussian Avatars. In *International Conference on 3D Vision (3DV)*.
- Denis Zorin, Peter Schröder, and Wim Sweldens. 1997. Interactive multiresolution mesh editing. In *Proceedings of the 24th annual conference on Computer graphics and interactive techniques*. 259–268.